

Mass and energy balance calculations for artificial ice reservoirs (Icestupas)

Suryanarayanan Balasubramanian^{1*}, Martin Hoelzle¹, Michael Lehning²,
Sonam Wangchuk³, Johannes Oerlemans⁴, Felix Keller^{5,6} and Jordi Bolíbar⁴

¹ University of Fribourg, Fribourg, Switzerland

² WSL Institute for Snow and Avalanche Research, Davos, Switzerland

³ Himalayan Institute of Alternatives Ladakh, Leh, India

⁴ Institute for Marine and Atmospheric Research, Utrecht University, Utrecht, The Netherlands

⁵ Academia Engiadina, Samedan, Switzerland

⁶ ETH, Zürich, Switzerland

Correspondence*:

Suryanarayanan Balasubramanian

suryanarayanan.balasubramanian@unifr.ch

2 ABSTRACT

Artificial Ice Reservoirs (AIRs) can successfully store water during winter and release the water during spring and summer. This makes them a reliable fresh water resource for irrigation in dry environments. Several AIRs have been built but studies of their water storage capacity and efficiency are scarce. This study models a cone-shaped AIR popularly called Icestupa. Processes involved in the development and temporal evolution of an Icestupa are calculated by a physically-based model using equations governing the heat transfer, vapour diffusion and transport of water that undergoes phase changes. These processes were quantified using meteorological data in conjunction with fountain spray information (mass input of an AIR) to estimate the quantity of frozen, melted, evaporated and runoff water for three sites in Switzerland and one in India. At these measurement sites, AIR were built for model validation purposes. The model was further tested by performing a sensitivity and uncertainty study showing that the most sensitive parameters are the ice emissivity and the temperature threshold used to determine precipitation phase. Model calculations estimate that the AIR stored about % of the total water sprayed as ice.

Keywords: iceshelf, mass balance, water storage, climate change adaptation, geoengineering

1 INTRODUCTION

Seasonal snow cover, glaciers and permafrost are expected to change their water storage capacity due to climate change with major consequences for downriver water supply (Immerzeel et al., 2019). The challenges brought about by these changes are especially important for dry mountain environments such as in Central Asia or the Andes, which directly rely on the seasonal meltwater for their farming and drinking needs (Hoelzle et al., 2019; Apel et al., 2018; Buytaert et al., 2017; Chen et al., 2016; Unger-Shayesteh et al., 2013). Some villages in Ladakh, India have already been forced to relocate due to glacial retreat and the corresponding loss of their main fresh water resources (Grossman, 2015).



Figure 1. Icestupa in Ladakh, India on March 2017 was 24 m tall and contained around 3700 m³ of water.
Picture Credits: Lobzang Dadul

24 Artificial ice reservoirs (AIRs) have been considered to be a feasible way to adapt to these changes (Hock
25 et al., 2019; Nüsser et al., 2019b). An AIR is a human-made ice structure typically constructed during the
26 cold winter months and designed to slowly release freshwater during the warm and dry spring and summer
27 months. The main purpose of AIRs is irrigation. Therefore, AIRs are designed to store water in the form of
28 ice as long into the summer as possible. The energy required to construct an AIR is usually derived from
29 the gravitational head of the source water body. Some are constructed horizontally by freezing water using
30 a series of checkdams and others are built vertically by spraying water through fountain systems (Nüsser
31 et al., 2019a). The latter are colloquially referred to as Icestupas and are the subject of this study.

32 A typical Icestupa just requires a pipeline attached to a vertically mounted metal pipe with a fountain
33 nozzle for construction. Their water source is usually a high altitude lake or glacial stream. Due to the
34 altitude difference between the pipeline input and fountain output, water ejects from the fountain nozzle as
35 droplets that eventually lose their latent heat to the atmosphere and accumulate as ice around the metal pipe.
36 The fountain nozzle is raised through addition of further pipes as and when significant ice accumulates.
37 Typically, a dome of branches is constructed around the metal pipe so that such pipe extensions can be
38 done from within this dome. During the winter, the fountain is manually activated from sunset to sunrise.
39 Threads, tree branches and fishing nets are used to guide and accelerate the ice formation.

40 Since their invention in 2013 (Wangchuk, 2014), Icestupas have gained widespread publicity in the region
41 of Ladakh, Northern India since they require very little infrastructure, skills and energy to be constructed
42 in comparison to other water storage technologies. Compared to other AIR geometries, Icestupas (Fig.
43 1) can be built at lower altitudes and last much longer into the summer than other types of ice structures
44 (Wangchuk, 2014). However, to date, no reliable estimates exist about the amount of sprayed water that
45 is necessary to create them and the meltwater they provide (Nüsser et al., 2019a). Rough estimates of
46 Icestupa meltwater in Ladakh suggest that the water loss during the construction process is considerable
47 (see Appendix 8.1). A complete set of measurements of the water storage and energy balance are required
48 to understand the cause of the water losses better and increase the construction efficiency.

49 In this paper, we aim to develop a physically-based model of a vertical AIR (or Icestupa) that can quantify
50 their storage efficiency using existing weather and water usage information. Mass and energy balance

Table 1. The Scientific AIR

AIR	Gangles, 2021	Guttannen, 2021	Guttannen, 2020	Schwarzsee, 2019
Code	IN21	CH21	CH20	CH19
Altitude [m a.s.l.]	4025	1047	1047	967
Fountain Duration	Jan 18 - Mar 10	Nov 22 - Feb 21	Jan 3 - Feb 27	Jan 30 - Feb 16
Drone Flights	6	9	3	0
r_{spray} [m]	10.8	6.9	7.7	1.2
V_{dome} [m ³]	78.5	13.2	23.9	0

51 equations were used to estimate the quantity of water frozen, melted, evaporated and runoff. Sensitivity
 52 and uncertainty analysis were performed to identify the most critical parameters and the variance caused
 53 by them. For validation, we chose four AIR built across the winters of 2019, 2020 and 2021 in India and
 54 Switzerland. Our model and validation experiments provide first steps towards evaluating the effectiveness
 55 of a vertical AIR for irrigation and allow us to outline some preliminary guidelines for consideration when
 56 a construction of an Icestupa for water storage is envisaged.

2 STUDY SITES

57 To accurately estimate and validate the ice volume of AIR the model requires three kinds of datasets
 58 namely, weather, water and ice volume. So through the winters of 2019, 2020 and 2021 several scientific
 59 AIR were constructed by teams in Switzerland and India. Each site had an Automatic Weather Station
 60 (AWS) nearby. Also drone flights were conducted periodically to record AIR ice volume. The model was
 61 applied on four of the AIR which have a relatively complete dataset associated with them as shown in
 62 Table 1. For brevity, only the model application on CH21 AIR is discussed below.
 63

2.1 CH21 AIR

64 The Guttannen (CH21) site in the Bern region lies at 1047 m a.s.l.. In the winter (Oct-Apr), mean daily
 65 minimum and maximum air temperatures vary between -13 and 15 °C. Clear skies are rare, averaging
 66 around 7 days during winter (Meteoblue, 2020). The site was situated adjacent to a stream resulting in high
 67 humidity values across the study period as shown in Fig. 2. The fountain used for spraying water had an
 68 initial height of 2.3 m. The water was transferred from a spring water source and flowed via a flowmeter to
 69 the nozzle. In addition, a webcam guaranteed a continuous survey of the site during the construction of the
 70 AIR.

71 The CH21 AIR was constructed by Guttannen Bewegt Association on a garden adjacent to a stream in
 72 Guttannen, Switzerland. To initiate the ice formation process, tree branches were laid covering the fountain
 73 pipe. The fountain height varied between 2 to 5 m during the construction period. Fountain operation was
 74 guided by temperature conditions.

2.1.1 Weather measurements

75 Air temperature, relative humidity, wind speed, pressure, longwave, shortwave direct and diffuse radiation
 76 are required to calculate the surface energy balance of an AIR. For the CH21 AIR, the weather data was
 77 primarily drawn from a meteoswiss AWS located 184 m away from the construction site. In addition, we
 78 used ERA5 reanalysis dataset (Copernicus Climate Change Service (C3S), 2017) for filling data gaps and
 79 adding data that were not measured directly as shown in Fig. 3. Near-surface humidity is not provided



Figure 2. Bird's eye view of the CH21 AIR

81 directly in ERA5 dataset, but from near-surface (2 m from the surface) temperature (T_{ERA5}) and dew point
 82 temperature (Tw_{ERA5}) the relative humidity (RH) at 2 m was calculated as:

$$RH = 100 \cdot \frac{e_{sat}(Tw_{ERA5})}{e_{sat}(T_{ERA5})} \quad (1)$$

83 where the saturation vapour pressure function e_{sat} is expressed with the Teten's formula (Tetens, 1930):

$$e_{sat}(T) = a_1 \cdot e^{(a_3 \cdot \frac{T}{T+273.16-a_4})} \quad (2)$$

84 with T in $^{\circ}\text{C}$ and the parameters set for saturation over water ($a_1 = 611.21$ Pa, $a_3 = 17.502$ and $a_4 =$
 85 32.19 K) according to Buck (1981). Zero wind speed values were recorded whenever snow accumulated
 86 on the ultrasonic wind sensor. It was assumed this was the cause when null wind speeds were observed
 87 continuously for atleast 3 hours. All such null values were replaced using the ERA5 dataset.

88 The ERA5 reanalysis dataset has a good correlation with lower elevation sites in Switzerland (Scherrer,
 89 2020). The ERA5 grid point chosen (Latitude $46^{\circ} 38' 24''$ N, Longitude $8^{\circ} 15' 00''$ E) for the CH21 site was
 90 around 3.6 km away from the actual site. All the ERA5 variables were therefore fitted with the meteoswiss
 91 dataset via linear regressions.

92 2.1.2 Discharge measurements

93 The water flow rate or discharge was measured via an ultrasonic sensor attached to the fountain supply
 94 pipeline. However, due to various malfunctions, the discharge measurements were very sparse and could not
 95 be extrapolated for the complete measurement period. Instead the discharge duration was first determined
 96 using the hourly webcam images of the CH21 site. The available discharge measurement was later used to
 97 determine the average discharge quantity (10 l/min) during these periods.

98 2.1.3 Ice volume measurements

99 Several Drone flights were conducted in every AIR site. The DEM generated through these flights were
 100 analysed to obtain the circumference and volume of the ice structure. The mean circumference measured

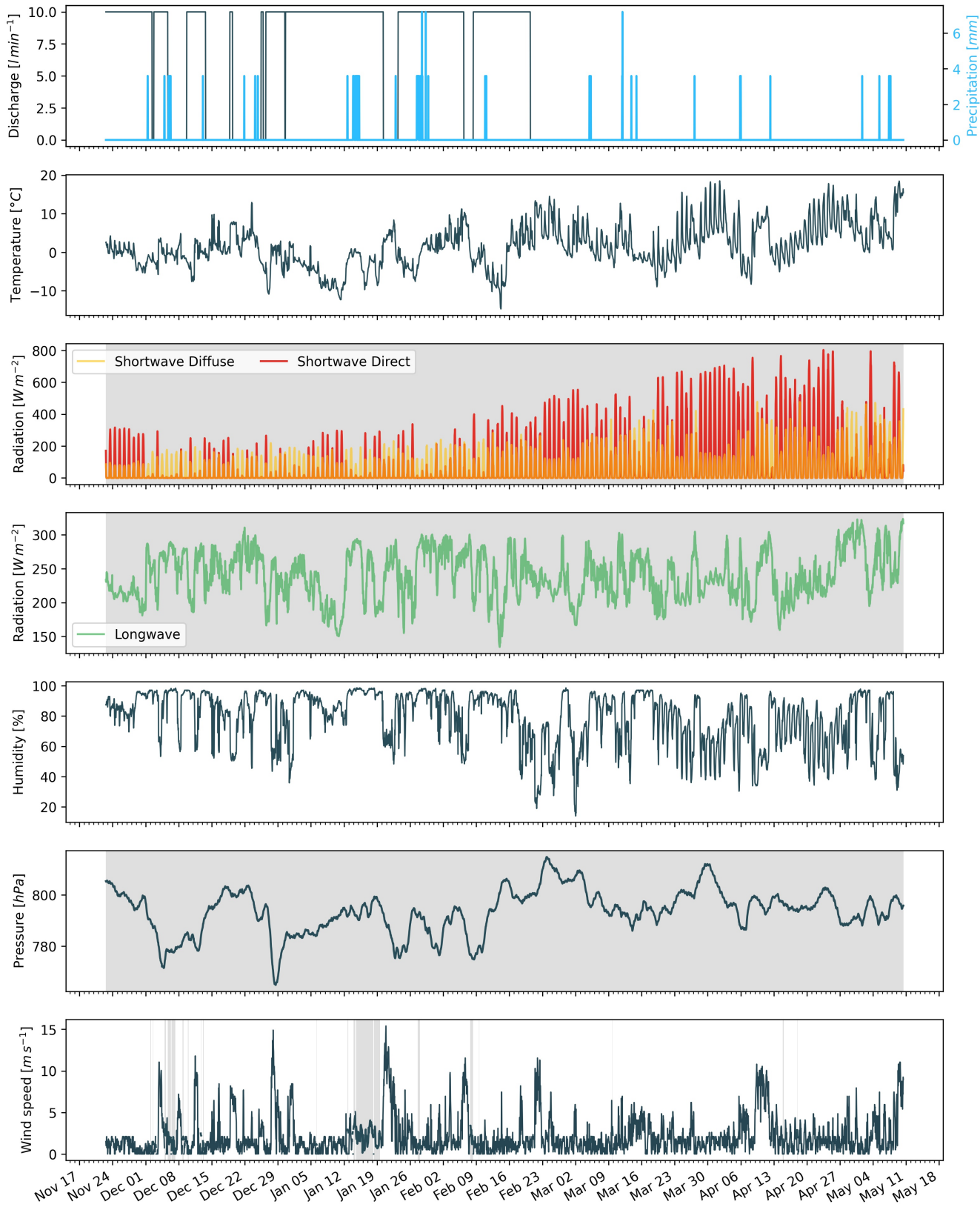


Figure 3. Measurements at the AWS of CH21 were used as main model input data in hourly frequency. Missing data, data gaps and errors were filled from the ERA5 dataset (shaded regions).

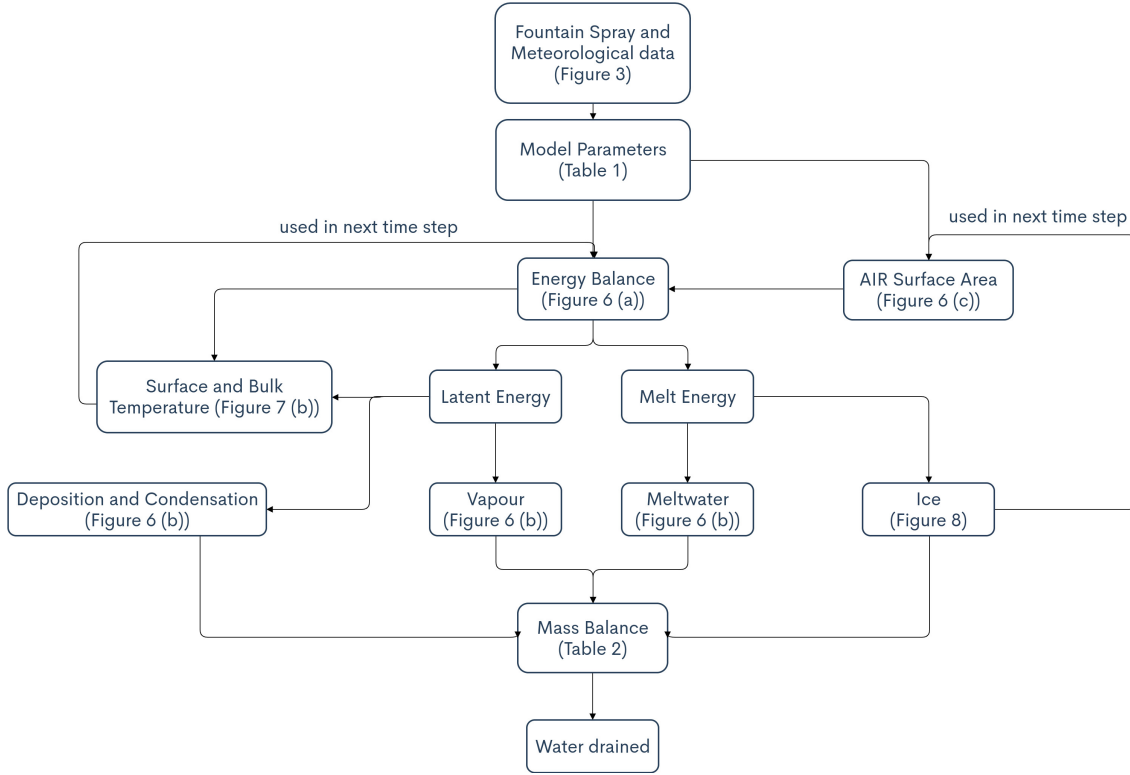


Figure 4. Model schematic showing the algorithm used in the model at every time step. Further details about the variables can be found in the associated tables and figures.

101 during the fountain duration was set as the spray radius (r_{spray}) and the first drone flight was used to set
 102 the dome volume (V_{dome}) for model initialisation. The ice volume data was later used for calibration and
 103 validation of the model.

104 The model application is restricted to CH21 AIR below. Model results and figures for other AIR can be
 105 found in the supplementary materials.

3 MODEL SETUP

106 A bulk energy and mass balance model is used to calculate the amounts of ice, meltwater, water vapour
 107 and runoff water of the AIR every hour. This model consists of four modules which estimates the AIR, a)
 108 geometric evolution , b) energy balance, c) surface temperature and d) mass balance.

3.1 Geometric evolution

110 Radius r_{ice}^i and height h_{ice}^i define the dimensions of the AIR assuming its geometry to be a cone. The
 111 surface area A^i exposed to the atmosphere and volume V^i are:

$$A = \pi \cdot r_{ice} \cdot \sqrt{r_{ice}^2 + h_{ice}^2} \quad (3)$$

$$V = \pi/3 \cdot r_{ice}^2 \cdot h_{ice} \quad (4)$$

112 Note that we do not specify the time step superscript i of the shape variables A , V , r_{ice} and h_{ice} for
 113 brevity. The equations used henceforth display model time step superscript i only if it is different from the
 114 current time step.

115 With the mass of the AIR M_{ice} , its current volume can also be expressed as:

$$V = M_{ice} / \rho_{ice} \quad (5)$$

116 where ρ_{ice} is the density of ice (917 kg m^{-3}).

117 The influence of the AIR fountain is parameterised by the fountain water temperature T_w and its spray
 118 radius r_{spray} . The initial radius r_0 of the AIR is assumed to be r_{spray} . The initial height h_0 depends on the
 119 dome volume V_{dome} used to construct the AIR as follows:

$$h_0 = \Delta x + \frac{3 \cdot V_{dome}}{\pi r_{spray}^2} \quad (6)$$

120 where Δx is the surface layer thickness (defined in Section 3.2)

121 During subsequent time steps, the dimensions of the AIR evolve assuming a uniform ice formation and
 122 decay across its surface area with an invariant slope $s_{cone} = \frac{h_{ice}}{r_{ice}}$. During these time steps, the volume is
 123 parameterised using Eqn. 4 as:

$$V = \frac{\pi \cdot r_{ice}^3 \cdot s_{cone}}{3} \quad (7)$$

124 However, the Icestupa cannot outgrow the maximum range of the water droplets ($(r_{ice})_{max} = r_F$).
 125 Combining equations 4, 6, 5 and 7, the geometric evolution of the Icestupa at each time step i can be
 126 determined by considering the following rules:

$$(r_{ice}, h_{ice}) = \begin{cases} (r_{spray}, h_0) & \text{if } i = 0 \\ (r_{ice}^{i-1}, \frac{3 \cdot M_{ice}}{\pi \cdot \rho_{ice} \cdot (r_{ice}^{i-1})^2}) & \text{if } r_{ice}^{i-1} \geq r_F \text{ and } \Delta M_{ice} > 0 \\ (\frac{3 \cdot M_{ice}}{\pi \cdot \rho_{ice} \cdot s_{cone}})^{1/3} \cdot (1, s_{cone}) & \text{otherwise} \end{cases} \quad (8)$$

127 where $\Delta M_{ice} = M_{ice}^{i-1} - M_{ice}^{i-2}$

128 3.2 Energy Balance

129 The energy balance equation (Hock, 2005) for the AIR is formulated as follows:

$$q_{SW} + q_{LW} + q_L + q_S + q_F + q_G = q_{surf} \quad (9)$$

130 where q_{surf} is the surface energy flux in [W m^{-2}]; q_{SW} is the net shortwave radiation; q_{LW} is the net
 131 longwave radiation; q_L and q_S are the turbulent latent and sensible heat fluxes. q_F represents the heat
 132 exchange of the fountain water droplets with the AIR ice surface. q_G represents ground heat flux between
 133 Icestupa surface and Icestupa interior. Energy transferred in the direction of the ice surface is always
 134 denoted as positive and away as negative.

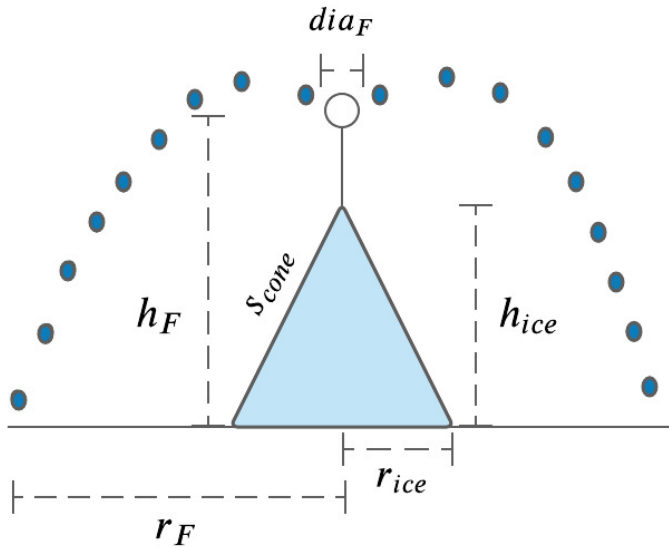


Figure 5. Shape variables and fountain constants of the CH21 Icestupa. r_{ice} is the radius, h_{ice} is the height and s_{cone} is the slope of the ice cone. r_{spray} is the spray radius, h_F is the height and dia_F is the nozzle diameter of the fountain.

135 Equation 9 is usually referred to as the energy budget for “the surface”, but practically it must apply
 136 to a surface layer of ice with a finite thickness Δx . The energy flux acts upon the Icestupa surface layer
 137 which has an upper and a lower boundary defined by the atmosphere and the ice body of the Icestupa,
 138 respectively. The parameter selection for Δx is based on the following two arguments: (a) the ice thickness
 139 Δx should be small enough to represent the surface temperature variations every model time step Δt and
 140 (b) Δx should be large enough for these temperature variations to not reach the bottom of the surface layer.
 141 Therefore, we introduced a 20 mm thick surface layer for a model time step of 1 hour, over which the
 142 energy balance is calculated. A sensitivity analysis was later performed to understand the influence of this
 143 factor. Here, we define the surface temperature T_{ice} to be the modelled average temperature of the Icestupa
 144 surface layer and the energy flux q_{surf} is assumed to act uniformly across the Icestupa area A .

3.2.1 Net Shortwave Radiation q_{SW}

146 The net shortwave radiation q_{SW} is computed as follows:

$$q_{SW} = (1 - \alpha) \cdot (SW_{direct} \cdot f_{cone} + SW_{diffuse}) \quad (10)$$

147 where SW_{direct} and $SW_{diffuse}$ are the ERA5 direct and diffuse short wave radiation, α is the modelled
 148 albedo and f_{cone} is the area fraction of the ice structure exposed to the direct shortwave radiation.

149 We model the albedo using a scheme described in Oerlemans and Knap (1998). The scheme records the
 150 decay of albedo with time after fresh snow is deposited on the surface. δt records the number of time steps
 151 after the last snowfall event. After snowfall, albedo changes over a time step, δt , as

$$\alpha = \alpha_{ice} + (\alpha_{snow} - \alpha_{ice}) \cdot e^{(-\delta t)/\tau} \quad (11)$$

152 where α_{ice} is the bare ice albedo value (0.35), α_{snow} is the snow ice albedo value (0.85) and τ is a decay
 153 rate, which determines how fast the albedo of the ageing snow reaches this value. The decay rate τ is
 154 assumed to have a base value of 10 days similar to values obtained by Schmidt et al. (2017) for wet surfaces
 155 and its maximal value is set based on observations by Oerlemans and Knap (1998) as shown in Table 2.
 156 Furthermore, the albedo α varies depending on the water source that formed the current Icestupa surface.
 157 Correspondingly, the albedo is reset to the value of bare ice albedo if the fountain is spraying water onto
 158 the current ice surface and to the value of fresh snow albedo if a snowfall event occurred. Snowfall events
 159 are assumed if the air temperature is below $T_{ppt} = 1^{\circ}C$ (Fujita and Ageta, 2000).

160 The area fraction f_{cone} of the ice structure exposed to the direct shortwave radiation depends on the
 161 shape considered. The direct solar radiation incident on the AIR surface is first decomposed into horizontal
 162 and vertical components using the solar elevation angle θ_{sun} . For a conical shape, half of the total curved
 163 surface is exposed to the vertical component of the direct shortwave radiation and the projected triangle
 164 of the curved surface is exposed to the horizontal component of the direct shortwave radiation. The solar
 165 elevation angle θ_{sun} used is modelled using the parametrisation proposed by Woolf (1968). Accordingly,
 166 f_{cone} is determined as follows:

$$f_{cone} = \frac{(0.5 \cdot r_{ice} \cdot h_{ice}) \cdot \cos\theta_{sun} + (\pi \cdot r_{ice}^2 / 2) \cdot \sin\theta_{sun}}{\pi \cdot r_{ice} \cdot (r_{ice}^2 + h_{ice}^2)^{1/2}} \quad (12)$$

167 The ERA5 diffuse shortwave radiation is assumed to impact the conical Icestupa surface uniformly.

168 3.2.2 Net Longwave Radiation q_{LW}

169 The net longwave radiation q_{LW} is determined as follows:

$$q_{LW} = LW_{in} - \sigma \cdot \epsilon_{ice} \cdot (T_{ice} + 273.15)^4 \quad (13)$$

170 where T_a represents the measured air temperature, T_{ice} is the modelled surface temperature, both
 171 temperatures are given in $^{\circ}C$, $\sigma = 5.67 \cdot 10^{-8} J m^{-2} s^{-1} K^{-4}$ is the Stefan-Boltzmann constant, LW_{in}
 172 denotes the incoming longwave radiation derived from the ERA5 dataset and ϵ_{ice} is the corresponding
 173 emissivity value for the Icestupa surface (see Table 2).

174 3.2.3 Turbulent sensible q_S and latent q_L heat fluxes

175 The turbulent sensible q_S and latent heat q_L fluxes are computed with the following expressions proposed
 176 by Garratt (1992):

$$q_S = c_a \cdot \rho_a \cdot p_a / p_{0,a} \cdot \frac{\kappa^2 \cdot v_a \cdot (T_a - T_{ice})}{(\ln \frac{h_{AWS}}{z_{ice}})^2} \quad (14)$$

$$q_L = 0.623 \cdot L_s \cdot \rho_a / p_{0,a} \cdot \frac{\kappa^2 \cdot v_a (p_{v,a} - p_{v,ice})}{(\ln \frac{h_{AWS}}{z_{ice}})^2} \quad (15)$$

177 where h_{AWS} is the measurement height above the ground surface of the AWS (in m), v_a is the wind
 178 speed in $[m s^{-1}]$, c_a is the specific heat of air at constant pressure ($1010 J kg^{-1} K^{-1}$), ρ_a is the air density
 179 at standard sea level ($1.29 kg m^{-3}$), $p_{0,a}$ is the air pressure at standard sea level ($1013 hPa$), κ is the

180 von Karman constant (0.4), L_s is the heat of sublimation (2848 kJ kg^{-1}) and z_{ice} (1.7 mm) denotes the
 181 roughness length of ice (momentum and scalar). The vapor pressures over air ($p_{v,a}$) and ice ($p_{v,ice}$) was
 182 obtained using the following formulation given in WMO (2018):

$$\begin{aligned} p_{v,a} &= 6.107 \cdot 10^{(7.5 \cdot T_a / (T_a + 237.3))} \\ p_{v,ice} &= (1.0016 + 3.15 \cdot 10^{-6} \cdot p_a - 0.074 \cdot p_a^{-1}) \cdot (6.112 \cdot e^{(22.46 \cdot T_{ice} / (T_{ice} + 272.62))}) \end{aligned} \quad (16)$$

183 where p_a is the measured air pressure in [hPa].

184 3.2.4 Fountain water heat flux q_F

185 The interaction between the fountain water and the ice surface is taken into account by assuming that
 186 the ice surface temperature remains constant at 0°C during time steps when the fountain is active. This
 187 process can be divided into two simultaneous steps: (a) the water temperature T_{water} is cooled to 0°C
 188 and (b) the ice surface temperature is warmed to 0°C . Process (a) transfers the necessary energy for
 189 process (b) throughout the fountain runtime. We further assume that this process is instantaneous, i.e. the
 190 ice temperature is immediately set to 0°C within just one time step Δt when the fountain is switched on.
 191 Thus, the heat flux caused by the fountain water is calculated as follows:

$$q_F = \begin{cases} 0 & \text{if } \Delta M_F = 0 \\ \frac{\Delta M_F \cdot c_{water} \cdot T_{water}}{\Delta t \cdot A} + \frac{\rho_{ice} \cdot \Delta x \cdot c_{ice} \cdot T_{ice}}{\Delta t} & \text{if } \Delta M_F > 0 \end{cases} \quad (17)$$

192 with c_{ice} as the specific heat of ice.

193 3.2.5 Bulk Icestupa heat flux q_G

194 The bulk Icestupa heat flux q_G corresponds to the ground heat flux in normal soils and is caused by the
 195 temperature gradient between the surface layer (T_{ice}) and the ice body (T_{bulk}). It is expressed by using the
 196 heat conduction equation as follows:

$$q_G = k_{ice} \cdot (T_{bulk} - T_{ice}) / l_{ice} \quad (18)$$

197 where k_{ice} is the thermal conductivity of ice ($2.123 \text{ W m}^{-1} \text{ K}^{-1}$), T_{bulk} is the mean temperature of the
 198 ice body within the Icestupa and l_{ice} is the average distance of any point in the surface to any other point in
 199 the ice body. T_{bulk} is initialised as 0°C and later determined from Eqn. 18 as follows:

$$T_{bulk}^{i+1} = T_{bulk} - (q_G \cdot A \cdot \Delta t) / (M_{ice} \cdot c_{ice}) \quad (19)$$

200 Since AIR's typically have conical shapes with $r_{ice} \gg h_{ice}$, we assume that the center of mass of the ice
 201 body is near the base of the fountain. Thus, the distance of every point in the AIR surface layer from the ice
 202 body's center of mass is between h_{ice} and r_{ice} . So we calculate q_G here assuming $l_{ice} = (r_{ice} + h_{ice})/2$.

203 3.3 Surface temperature

204 The available energy q_{surf} can act on the surface of the AIR to a) change its temperature, b) melt ice or
 205 c) freeze ice. So Eqn. 9 can be rewritten as:

$$q_{surf} = q_{freeze/melt} + q_T \quad (20)$$

Table 2. Free parameters in the model categorised as constant, uncertain and site parameters. Base value (B) and uncertainty (U) were taken from the literature. For assumptions (assum.), the uncertainty was chosen to be relatively large (5 %). For measurements (meas.), the uncertainty due to parallax errors is chosen to be (1 %).

Constant Parameters	Symbol	Value	References
Van Karman constant	κ	0.4	B: Cuffey and Paterson
Stefan Boltzmann constant	σ	$5.67 \cdot 10^{-8} W m^{-2} K^{-4}$	B: Cuffey and Paterson
Air pressure at sea level	$p_{0,a}$	1013 hPa	B: Mölg and Hardy
Density of water	ρ_w	$1000 kg m^{-3}$	B: Cuffey and Paterson
Density of ice	ρ_{ice}	$917 kg m^{-3}$	B: Cuffey and Paterson
Density of air	ρ_a	$1.29 kg m^{-3}$	B: Mölg and Hardy
Specific heat of ice	c_{ice}	$2097 J kg^{-1} ^\circ C^{-1}$	B: Cuffey and Paterson
Specific heat of water	c_w	$4186 J kg^{-1} ^\circ C^{-1}$	B: Cuffey and Paterson
Specific heat of air	c_a	$1010 J kg^{-1} ^\circ C^{-1}$	B: Mölg and Hardy
Thermal conductivity of ice	k_{ice}	$2.123 W m^{-1} K^{-1}$	B: Bonales et al.
Latent Heat of Sublimation	L_s	$2848 kJ kg^{-1}$	B: Cuffey and Paterson
Latent Heat of Fusion	L_f	$334 kJ kg^{-1}$	B: Cuffey and Paterson
Uncertain Parameters		Range	
Precipitation	T_{ppt}	$1 ^\circ C$	$\pm 1 ^\circ C$
Temperature threshold			B + U: Fujita and Ageta, Zhou et al.
Ice Emissivity	ϵ_{ice}	0.95	[0.949, 0.993]
Ice Albedo	α_{ice}	0.35	$\pm 5 \%$
Snow Albedo	α_{snow}	0.85	$\pm 5 \%$
Albedo Decay Rate	τ	10 days	[1, 22] days
Surface layer thickness	Δx	20 mm	$\pm 5 \%$

206 where q_T , q_{freeze} and q_{melt} represent energy associated with process (a), (b) and (c) respectively.

207 To distribute the surface energy flux into these three components, we categorize the model time steps
208 as freezing or melting events. Freezing events can only occur if there is fountain water available and the
209 surface energy flux is negative. But just these two conditions are not sufficient as the latent heat energy
210 can only contribute to temperature fluctuations. So to prevent latent heat energy from turning a melting
211 event into a freezing event an additional condition namely $(q_{surf} - q_L) < 0$ is required. Thus, freezing and
212 melting events are identified as follows:

$$q_{freeze/melt} = \begin{cases} q_{freeze} & \text{if } \Delta M_F > 0 \text{ and } q_{surf} < 0 \text{ and } (q_{surf} - q_L) < 0 \\ q_{melt} & \text{otherwise} \end{cases} \quad (21)$$

213 During a freezing event, the available energy $(q_{surf} - q_L)$ can either be sufficient or insufficient to
214 freeze the fountain water available. If insufficient, the additional energy further cools down the surface
215 temperature. So the surface energy flux distribution during a freezing event can be represented as:

$$(q_{freeze}, q_T) = \begin{cases} (q_{surf} - q_L, q_L) & \text{if } \Delta M_F \geq -\frac{(q_{surf} - q_L)A \cdot \Delta t}{L_f} \\ \left(\frac{\Delta M_F \cdot L_f}{A \cdot \Delta t}, q_{surf} + \frac{\Delta M_F \cdot L_f}{A \cdot \Delta t}\right) & \text{if } \Delta M_F < -\frac{(q_{surf} - q_L)A \cdot \Delta t}{L_f} \end{cases} \quad (22)$$

216 During a melting event, the surface energy flux (q_{surf}) is first used to change the surface temperature to
 217 T_{temp} calculated as:

$$T_{temp} = \frac{q_{surf} \cdot \Delta t}{\rho_{ice} \cdot c_{ice} \cdot \Delta x} + T_{ice} \quad (23)$$

218 If $T_{temp} > 0^\circ C$, then energy is reallocated from q_T to q_{melt} to maintain surface temperature at melting
 219 point. So the surface energy flux distribution during a melting event can be represented as:

$$(q_{melt}, q_T) = \begin{cases} (0, q_{surf}) & \text{if } T_{temp} < 0 \\ \left(\frac{T_{temp} \cdot \rho_{ice} \cdot c_{ice} \cdot \Delta x}{\Delta t}, q_{surf} - \frac{T_{temp} \cdot \rho_{ice} \cdot c_{ice} \cdot \Delta x}{\Delta t}\right) & \text{if } T_{temp} > 0 \end{cases} \quad (24)$$

220 3.4 Mass Balance

221 The mass balance equation for an AIR is represented as:

$$\frac{\Delta M_F + \Delta M_{ppt} + \Delta M_{dep}}{\Delta t} = \frac{\Delta M_{ice} + \Delta M_{water} + \Delta M_{sub} + \Delta M_{runoff}}{\Delta t} \quad (25)$$

222 where M_F is the discharge of the fountain; M_{ppt} is the cumulative precipitation; M_{dep} is the cumulative
 223 accumulation through water vapour deposition; M_{ice} is the cumulative mass of ice; M_{water} is the cumulative
 224 mass of melt water; M_{sub} represents the cumulative water vapor loss by sublimation and M_{runoff} represents
 225 the fountain discharge runoff that did not interact with the AIR. The LHS of equation 25 represents the rate
 226 of mass input and the RHS represents the rate of mass output for an AIR.

227 Precipitation input is calculated as shown in equation 26a where ρ_w is the density of water (1000
 228 $kg m^{-3}$), ppt is the measured precipitation rate in [$m s^{-1}$] and T_{ppt} is the temperature threshold below
 229 which precipitation falls as snow. Here, snowfall events were identified using T_{ppt} as $1^\circ C$. Snow mass
 230 input is calculated by assuming a uniform deposition over the entire circular footprint of the Icestupa.

231 The latent heat flux is used to estimate either the evaporation and condensation processes or sublimation
 232 and deposition processes as shown in equation 26b. During time steps at which surface temperature is
 233 below $0^\circ C$ only sublimation and deposition can occur, but if the surface temperature reaches $0^\circ C$,
 234 evaporation and condensation can also occur. As the differentiation between evaporation and sublimation
 235 (and condensation and deposition) when the air temperature reaches $0^\circ C$ is challenging, we assume
 236 that negative (positive) latent heat fluxes correspond only to sublimation (deposition), i.e. no evaporation
 237 (condensation) is calculated.

238 Since we have categorized every time step as a freezing and melting event, we can determine the meltwater
 239 and ice generated using the associated energy fluxes as shown in equations 26c and 26d. Having calculated
 240 all the other mass components the fountain wastewater generated every time step can be calculated using
 241 equation 26e.

$$\frac{\Delta M_{ppt}}{\Delta t} = \begin{cases} \pi \cdot r_{ice}^2 \cdot \rho_w \cdot ppt & \text{if } T_a < T_{ppt} \\ 0 & \text{if } T_a \geq T_{ppt} \end{cases} \quad (26a)$$

$$\left(\frac{\Delta M_{dep}}{\Delta t}, \frac{\Delta M_{sub}}{\Delta t} \right) = \begin{cases} \frac{q_L \cdot A}{L_s} \cdot (1, 0) & \text{if } q_L \geq 0 \\ \frac{q_L \cdot A}{L_s} \cdot (0, -1) & \text{if } q_L < 0 \end{cases} \quad (26b)$$

$$\frac{\Delta M_{water}}{\Delta t} = \frac{q_{melt} \cdot A}{L_f} \quad (26c)$$

$$\frac{\Delta M_{ice}}{\Delta t} = \frac{q_{freeze} \cdot A}{L_f} + \frac{\Delta M_{ppt}}{\Delta t} + \frac{\Delta M_{dep}}{\Delta t} - \frac{\Delta M_{sub}}{\Delta t} - \frac{\Delta M_{melt}}{\Delta t} \quad (26d)$$

$$\frac{\Delta M_{runoff}}{\Delta t} = \frac{\Delta M_F - \Delta M_{ice}}{\Delta t} \quad (26e)$$

242 To estimate the mass of any component at time step i , one can now sum the mass flux estimated above:

$$M_{comp}^i = \sum_{t=0}^{t=i} \left(\frac{\Delta M_{comp}}{\Delta t} \right)_t + M_{comp}^0 \quad (27)$$

243 where

$$M_{comp}^0 = \begin{cases} -V_{dome} * \rho_{ice} & \text{if } M_{comp} = M_{ice} \text{ or } M_F \\ 0 & \text{otherwise} \end{cases} \quad (28)$$

244 Considering AIRs as water reservoirs, we can quantify their potential through the amount of water they
245 store (storage quantity) and the length of time they store it (storage duration). Another means of comparing
246 different Icestupas is through their water storage efficiency defined accordingly as:

$$\text{Storage Efficiency} = \frac{M_{water}}{(M_F + M_{ppt} + M_{dep})} \cdot 100 \quad (29)$$

4 MODEL RESULTS

247 The model was forced with meteorological data from 22nd November to 10th May 2021 (Fig. 3) and
248 various parameters (see Table 2) to calculate the mass and energy balance of the CH21 AIR.

249 4.1 Energy and mass balance calculation

250 Daily averages of some components of the energy balance are shown in Fig. 6 (b). On average during
251 the experiment duration, the total energy balance was almost zero. Net shortwave radiation (35 W m^{-2}),
252 sensible (41 W m^{-2}) and latent heat flux (2 W m^{-2}) with a mostly positive flux towards the surface of the
253 icestupa were compensated by the net longwave radiation (- 47 W m^{-2}), the fountain water heat flux (-
254 13 W m^{-2}) and the freeze/melt energy (- 19 W m^{-2}). The contributions of other fluxes were negligible in
255 comparison.

256 Net shortwave radiation is the main input to, and the most varying energy flux on the ice surface. Its
257 variability is controlled by the surface albedo α and the area fraction f_{cone} which therefore represent key
258 variables in the energy balance (Fig. 7 (b)). Although global radiation flux reached a daily maximum value

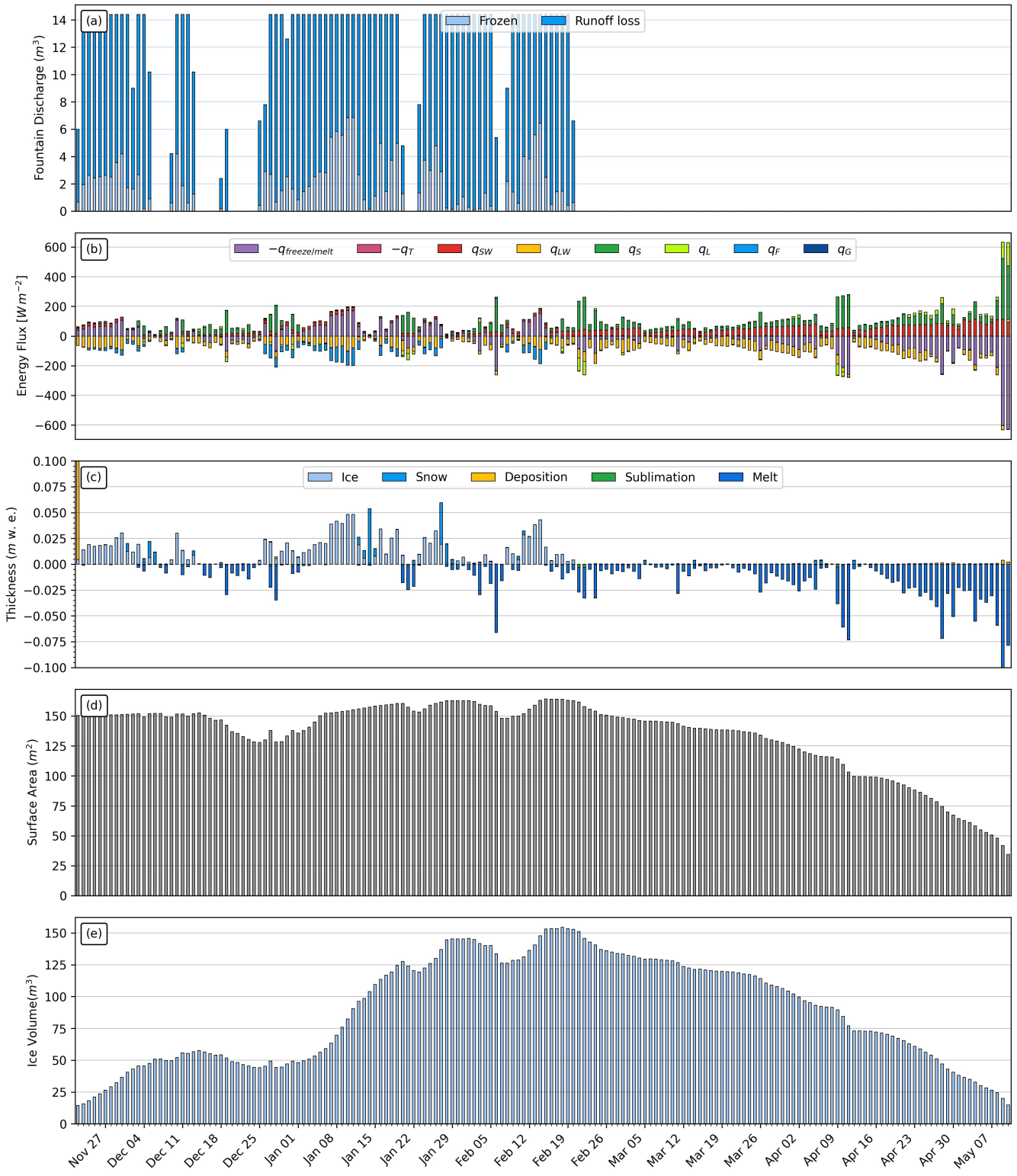


Figure 6. (a) Fountain discharge (b) energy flux components, (c) mass flux components (d) surface area and (e) volume of the Icestupa in daily time steps. q_{SW} is the net shortwave radiation; q_{LW} is the net longwave radiation; q_L and q_S are the turbulent latent and sensible heat fluxes. q_F represents the interactions of the fountain water with the AIR surface layer. q_G quantifies the heat conduction process between the AIR surface layer and the ice body.

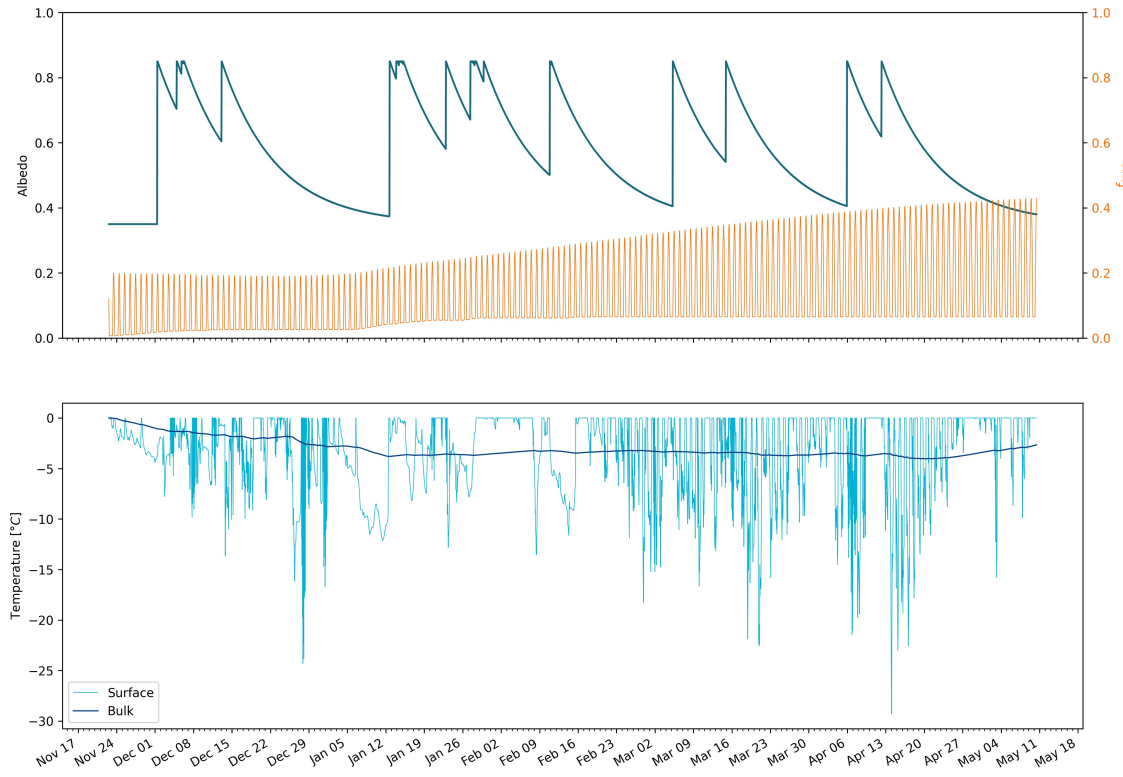


Figure 7. Some derived parameters of the model, namely, albedo and f_{cone} (a), Surface and bulk temperature (b). In (a), the green curve shows how snow and fountain-on events reset albedo between ice albedo and snow albedo. The decay of the snow albedo to ice albedo can also be observed. The orange curve shows how the solar radiation area fraction varied diurnally with variations in the solar elevation angle. In (b), the surface temperature (light blue curve) was forced to be $0\text{ }^{\circ}\text{C}$ during fountain activity. The corresponding bulk temperature is shown with the dark blue curve.

of $340\text{ }Wm^{-2}$, q_{SW} only went up to $114\text{ }Wm^{-2}$. This is caused by the fact that less than 40 % of the direct solar radiation influenced the Icestupa surface as shown by the area fraction f_{cone} in Fig. 7 (a). Snowfall is the atmospheric variable connected most closely and proportionally to albedo. Higher and/or more frequent snowfall thus decreases the energy available for melt due to the corresponding increase in α .

q_{LW} was predominantly negative indicating that this energy balance component drove the freezing of the ice structure. Daily values of q_{LW} ranged from -101 to $19\text{ }Wm^{-2}$. Turbulent sensible heat flux q_S contributed mostly to the melt of the ice structure. Daily values of q_S ranged from -3 to $410\text{ }Wm^{-2}$. Daily values of the turbulent latent heat flux q_L ranged from -90 to $157\text{ }Wm^{-2}$. Since the mean of q_L was positive, the Icestupa gained mass cumulatively from the atmosphere due to the deposition process. Daily values of fountain water heat flux ranged from -119 to $4\text{ }Wm^{-2}$. q_F was also a significant contributor to the freezing process like q_{LW} . So the influence of the fountain on the energy balance and the freezing events was significant. The contribution of heat flux by conduction q_G was minimal as it only varied between -1 to $3\text{ }Wm^{-2}$ with a mean of $0\text{ }Wm^{-2}$. The energy contributing to surface temperature changes (q_T) was insignificant in comparison to the energy spent on freezing and melting ($q_{freeze/melt}$). The resulting bulk temperature and the surface temperature are shown in Fig. 7 (b). For the total considered period, $q_{freeze/melt}$ accounted for 30% of overall energy turnover. The energy turnover is calculated as the sum of energy fluxes in absolute values. q_{LW} accounted for 22%, followed by q_S (20%), q_{SW} (16%), q_L (5%), q_F (6%), q_T (1%) and q_G (0%).

Table 3. Summary of mass balance components for the CH21 AIR at the end of the model run on 10th May 2021.

Component		CH21
Input	M_F	1,000,041
	M_{ppt}	29,533
	M_{dep}	4,755
Output	M_{water}	196,011
	M_{ice}	12,304
	M_{sub}	4,747
	M_{runoff}	821,267

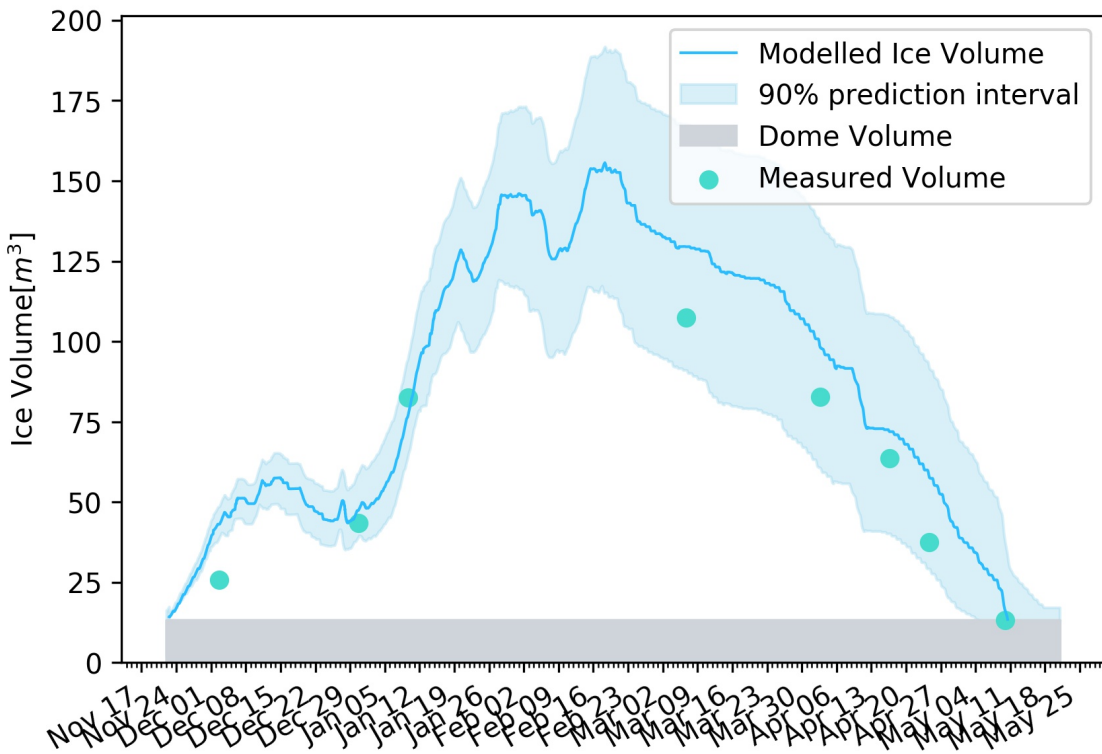


Figure 8. Modelled ice volume during the lifetime of the CH21 AIR (blue curve). Green points indicate the validation measurements. The prediction interval is based on the ice volume uncertainty caused by the most sensitive parameters, namely, temperature threshold below which precipitation falls as snow and the ice emissivity.

Fig. 6 (c) represents the mass fluxes associated with these energy exchanges expressed in m w.e. It shows the ice and meltwater formed due to q_{melt} , snow accumulated due to precipitation, water vapour deposition and sublimation due to q_L .

The total water used for the Icestupa development includes contributions from the fountain (96.7%), snowfall (2.9 %), deposition (0.5 %) as shown in Table 3. Therefore, in the case of CH21 we used a water input of 1,034,328 kg, with a resultant storage efficiency of 19 %.

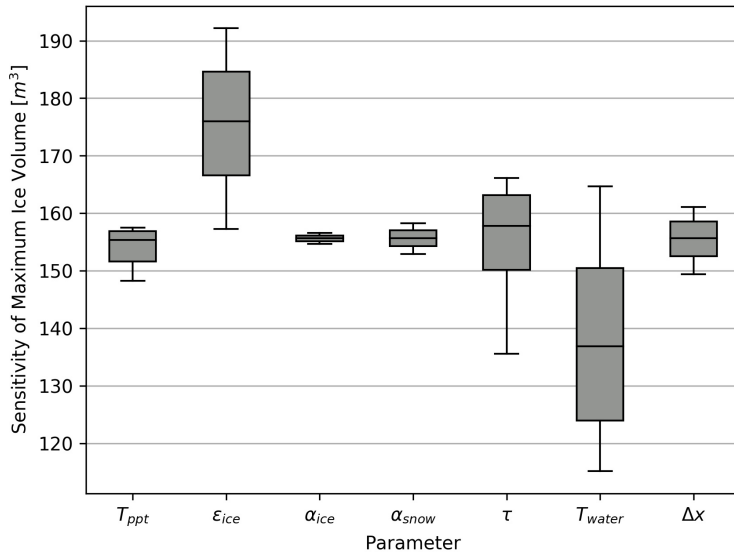


Figure 9. Sensitivities of maximum ice volume to all the uncertain and site parameters used in the model (Table 2).

5 MODEL SENSITIVITY AND UNCERTAINTY ANALYSIS

283 The icestupa model can be regarded as a function $f(x_1, x_2 \dots, x_n) = (y_1, y_2 \dots, y_m)$, where
 284 ($x_1, x_2 \dots, x_n$) are the model parameters and ($y_1, y_2 \dots, y_m$) are the model outputs. The influence of each
 285 parameter on the output variables of interest were quantified and the most important physical parameters
 286 for the subsequent uncertainty analysis were determined. The sensitivity of a parameter x_j is determined
 287 by keeping all other parameters $x_i, i \neq j$ fixed at their baseline value and varying x_j within values that are
 288 physically plausible.

289 A sensitivity study on the parameters (listed in Table 2) was performed with the maximum ice volume
 290 as the target variable. All the parameters were assumed to be independent of each other with a uniform
 291 distribution. This assumption ignores the auto-correlation present among the parameters associated with
 292 the albedo parameterisation. The range of uncertain parameters were set based on available literature values
 293 or varied $\pm 5\%$ from the base value if no such reference was available. The uncertainty of all the site
 294 parameters were caused due to parallax errors during manual measurement. This was quantified with a
 295 range of $\pm 1\%$ from the base value. However, it must be kept in mind that, even though intended to be as
 296 objective as possible, the selection of a parameter range has a subjective part that influences the results and
 297 conclusions obtained in this analysis. The variation of the model outputs y_k is evaluated to quantify the
 298 local sensitivities $s_{j,k}$ that are defined here as the 95% range of the simulated outputs.

299 To perform the uncertainty analysis, we included only parameters that influence the maximum ice volume
 300 by at least $0.1 m^3$. All other parameters were fixed at their baseline value. Fig. 9 shows all the variance
 301 produced by these uncertain parameters in maximum ice volume calculation.

302 In total, the sensitivity analysis required 120 simulations, and the uncertainty analysis a total of 662
 303 simulations.

Table 4. AIR Results

AIR	IN21	CH21	CH20	CH19
Max Ice Volume [m^3]	703	156	107	1
Storage Efficiency [%]	18	19	14	3
Storage Duration [days]	?	169	93	45
Validation RMSE [m^3]	59	13	25	0.2

6 DISCUSSION

304 **6.1 Important assumptions**

305 In the sensitivity and uncertainty analysis presented above, we did not account for several general
 306 assumptions and parametrisation choices that may cause model errors. Some assumptions and their
 307 potential to cause errors are discussed below.

- 308 • Turbulent Sensible and Latent Heat Fluxes: The method used to calculate the turbulent heat fluxes
 309 by Garratt (1992) assumes that the turbulent heat fluxes are acting over a uniform planar surface to
 310 determine the roughness length. Since our application is on a conical surface, the distance to the ice
 311 surface is not uniform and well defined. Hence, z_{ice} has no real physical significance here.
- 312 • Droplet flight time loss: Water losses during the flight time of fountain droplets were neglected making
 313 all the fountain spray available for freezing. For the CH21 experiment, inclusion of this parameter does
 314 not influence results since it is already accounted for in the runoff water discharge rate which was at
 315 least $3 l \text{ min}^{-1}$.
- 316 • Nucleation of droplets: Corresponding to droplet flight time, ice/snow formation is also possible before
 317 surface contact if nucleation occurs during flight time. For the CH21 experiment, this process will
 318 further increase the freeze rate and hence the storage efficiency. This process is neglected for model
 319 simplicity.
- 320 • Shape Effects: The suppression of heat exchange between the snow/ice surface and the air adjacent
 321 to the surface effectively slows down snow/ice ablation in spring and promotes the stagnation of the
 322 cold air within topographical depressions (Fujita et al., 2010). The quantitative contribution of the
 323 atmospheric decoupling over melting snow/ice for the total mass and energy balance is ignored in the
 324 model.

7 CONCLUSIONS

325 We outlined a methodology for estimating ice, liquid water, water vapour and runoff quantities produced
 326 during the construction of an AIR using measurements of fountain spray rate, air temperature, radiation,
 327 humidity, pressure, wind and cloudiness at four different study sites. The comparison with all the validation
 328 measurements at two different dates during the experiment led to satisfying results as shown in Table 4.

329 The model results support the hypothesis that there could be considerable water loss during the formation
 330 of AIR particularly due to excessive fountain spray. Further experiments at different locations with different
 331 fountains are required to better understand the influence of construction decisions on the results.

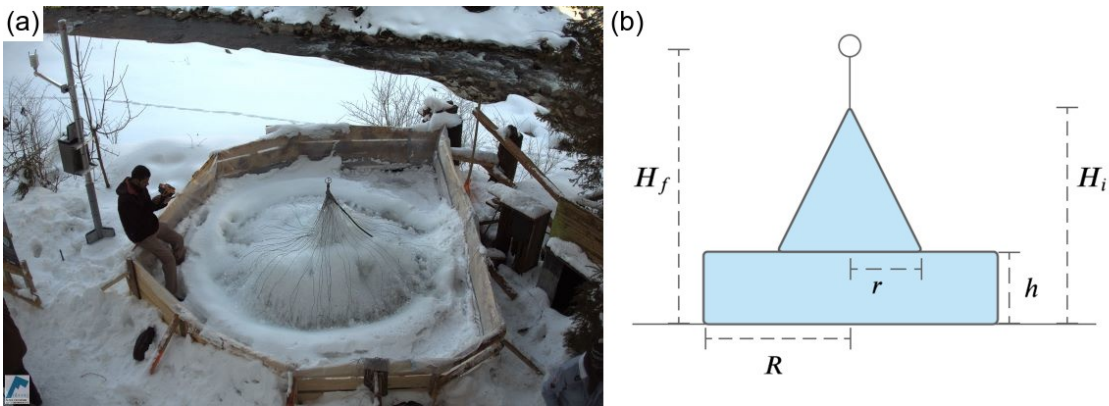


Figure 10. (a) The ice structure during the first validation measurement as seen on the webcam image of 14th Feb. (b) The corresponding cross section of the EP ice structure with the field estimates of r, R, h, H_i, H_f used to determine the Icestupa volume is shown on the right.

8 APPENDIX

8.1 Ladakh Icestupa 2014/15

A 20 m tall Icestupa (Wangchuk, 2015c) was built in Phyang village, Ladakh at an altitude of 3500 m a.s.l. Assuming a conical shape with a diameter of 20 m, the corresponding volume of this Icestupa becomes 2093 m^3 or 1,920 m^3 w.e. The fountain sprayed water at a rate of 210 $l\ min^{-1}$ (Wangchuk, 2015e) from 21st January (Wangchuk, 2015a) to at least until 5th March 2015 (Wangchuk, 2015b) (around 43 nights). Assuming fountain spray was active for 8 hours each night, we estimate water consumption to be around 4,334 m^3 . Thus, during the construction/freezing period of the Icestupa, roughly 56 % of the water provided was wasted. The actual water loss is bound to be much higher due to further vapour losses during the melting period. This Icestupa completely melted away on 6th July 2015 (Wangchuk, 2015d). Therefore, the storage duration was 166 days or roughly 5 months.

8.2 CH19 AIR

The CH19 AIR in the Schwarzsee region lies at 967 m a.s.l.. In the winter (Oct-Apr), mean daily maximum and minimum air temperatures vary between -4 and 14 °C. Clear skies are rare, averaging around 7 days, and precipitation amounts average 155 mm per month during winter (Meteoblue, 2020). The site was situated adjacent to a stream resulting in high humidity values across the study period. Within the EP site, an enclosure with a 1.8 m radius was constructed for the experiment. An automatic weather station (AWS) was adjacent to the wooden boundary as shown in Fig. ???. The fountain used for spraying water had a nozzle diameter of 5 mm and a height of 1.35 m, and was placed in the centre of the wooden enclosure. The water was transferred from a spring water source at 1267 m a.s.l. by pipeline and flowed via a flowmeter and an air escape valve to the nozzle, where it was sprinkled with a spray radius of around 1.7 m. The air escape valve was installed to avoid errors in the flow measurements due to air bubbles. In addition, a webcam guaranteed a continuous survey of the site during the construction of the Icestupa.

8.2.1 Weather data

Precipitation data was derived from the Plaffeien AWS (IDAWEB, 2019) located 8.8 km away from the measurement site at an altitude of 1042 m a.s.l. We recognised during our data analysis that, except precipitation, all the other meteorological variables of the EP site correlated much better with the ERA5 dataset than the nearby Plaffeien AWS dataset. The 2 m temperature parameter correlated with air temperature ($r^2 = 0.9$), surface pressure parameter correlated with air pressure ($r^2 = 1$) and 10m

360 wind speed parameter (derived from horizontal and vertical components) correlated with wind speed
 361 ($r^2 = 0.6$) .

362 Due to a power failure, all data from the EP AWS was lost from 27th February 15:20 2019 to 2nd March
 363 15:00 2019 (equivalent to around 7% of the measurement period). During heavy snowfall events, the
 364 ultrasonic wind sensor was blocked and recorded zero values. ERA5 was used to fill such errors and data
 365 gaps .

366 The ERA5 grid point chosen (Latitude 46° 38' 24" N, Longitude 7° 14' 24" E) for the EP site was around
 367 9 km away from the actual site. All the ERA5 variables were therefore fitted with the EP dataset via linear
 368 regressions. With the modified ERA5 dataset, we were also able to further extend the EP dataset and allow
 369 the model to run beyond 18th March 2019. Precipitation was filled as null values beyond 18th March 2019.
 370

8.2.2 Fountain spray radius of CH19 AIR

371 This fountain spray radius is determined by modelling the projectile motion of the water droplets. Using
 372 mass conservation, the droplet speed v_F can be determined from the spray rate d_F and the diameter dia_F
 373 of the nozzle as follows:

$$v_F = \frac{d_F}{\pi \cdot dia_F^2 / 4} \quad (30)$$

374 Afterwards, we assume that the water droplets move with an air friction free projectile motion from
 375 the fountain nozzle with a height h_F to the ice/ground surface. The resulting spray radius r_F was then
 376 determined from the projectile motion equation as follows:

$$r_F = \frac{v_F \cdot \cos\theta_F (v_F \cdot \sin\theta_F + \sqrt{(v_F \cdot \sin\theta_F)^2 + 2 \cdot g \cdot h_F})}{g} \quad (31)$$

377 where $g = 9.8 \text{ m s}^{-2}$ is the acceleration due to gravity and $\theta_F = 45^\circ$ is the angle of launch.

8.2.3 CH19 Field Measurements for validation

379 The volume was determined by decomposing the ice structure into a cylinder (length $2R$ and height h)
 380 and a cone (radius r and height $(H_i - h)$) through the following equation:

$$V = \pi \cdot R^2 \cdot h + 1/3 \cdot \pi \cdot r^2 \cdot (H_i - h) \quad (32)$$

381 Manual measurements were performed at the end of the freezing period on 14th February 16:00 2019
 382 (only one more fountain run was possible after this date) to estimate r, R, h, H_i, H_f (see Fig. ?? for the
 383 different geometry components):

$$0.55 \leq r \leq 1m ; 1.1 \leq R \leq 1.2m ; 0.1 \leq h \leq 0.2m ; 0.6 \leq H_i \leq 0.8m ; 1.3 \leq H_f \leq 1.4m$$

384 The ranges of the variables show the variance of the Icestupa's dimensions across different compass
 385 orientations. Correspondingly, the volume range estimated for the first validation point was 0.857 ± 0.186
 386 m^3 on 14th February 16:00 2019.

387 The second validation point corresponds to the end of the melting process on 10th March 18:00 2019.
388 Based on the webcam imagery and manual measurement, a thin layer of ice with an observed thickness
389 between 0.01 to 0.06 m could be quantified. This results in the volume range for the second validation to
390 be $0.13 \pm 0.09 \text{ m}^3$ on 11th March 2019

391 In reality, the EP ice structure was more cylindrical until a height of 0.2 m and conical afterwards until a
392 height of 0.6 m with a radius of 1.18 m. However, we assume a conical shape of this ice structure in order
393 to apply the modelling strategy described below.

REFERENCES

- 394 Apel, H., Abdykerimova, Z., Agalhanova, M., Baimaganbetov, A., Gavrilko, N., Gerlitz, L., et al. (2018).
395 Statistical forecast of seasonal discharge in central asia using observational records: development of a
396 generic linear modelling tool for operational water resource management. *Hydrology and Earth System
397 Sciences* 22, 2225–2254. doi:10.5194/hess-22-2225-2018
- 398 Bonales, L. J., Rodriguez, A. C., and Sanz, P. D. (2017). Thermal conductivity of ice prepared under
399 different conditions. *International Journal of Food Properties* 20, 610–619. doi:10.1080/10942912.
400 2017.1306551
- 401 Buck, A. L. (1981). New equations for computing vapor pressure and enhancement factor. *Journal of
402 Applied Meteorology and Climatology* 20, 1527 – 1532
- 403 Buytaert, W., Moulds, S., Acosta, L., Bievre, B. D., Olmos, C., Villacis, M., et al. (2017). Glacial melt
404 content of water use in the tropical andes. *Environmental Research Letters* 12, 114014. doi:10.1088/
405 1748-9326/aa926c
- 406 Chen, Y., Li, W., Deng, H., Fang, G., and Li, Z. (2016). Changes in central asia's water tower: Past, present
407 and future. *Nature* doi:10.1088/1748-9326/aa926c
- 408 [Dataset] Copernicus Climate Change Service (C3S) (2017). Era5: Fifth generation ecmwf atmospheric
409 reanalyses of the global climate. [Available at [https://cds.climate.copernicus.eu/
410 cdsapp#!/home](https://cds.climate.copernicus.eu/cdsapp#!/), accessed 2019-10-01]
- 411 Cuffey, K. M. and Paterson, W. S. B. (2010). *The Physics Of Glaciers* (Elsevier)
- 412 Fujita, K. and Ageta, Y. (2000). Effect of summer accumulation on glacier mass balance on the
413 tibetan plateau revealed by mass-balance model. *Journal of Glaciology* 46, 244–252. doi:10.3189/
414 172756500781832945
- 415 Fujita, K., Hiyama, K., Iida, H., and Ageta, Y. (2010). Self-regulated fluctuations in the ablation of a snow
416 patch over four decades. *Water Resources Research* 46, W11541. doi:10.1029/2009WR008383
- 417 Garratt, J. R. (1992). *The Atmospheric Boundary Layer* (Cambridge University Press)
- 418 Grossman, D. (2015). As himalayan glaciers melt, two towns face the fallout [Available at
419 [https://e360.yale.edu/features/as_himalayan_glaciers_melt_two_towns_
420 face_the_fallout](https://e360.yale.edu/features/as_himalayan_glaciers_melt_two_towns_face_the_fallout), accessed 2019-10-01]
- 421 Hock, R. (2005). Glacier melt: a review of processes and their modelling. *Progress in Physical Geography:
422 Earth and Environment* 29, 362–391
- 423 Hock, R., Rasul, G., Adler, C., Cáceres, B., Gruber, S., Hirabayashi, Y., et al. (2019). 2019: High mountain
424 areas. *IPCC Special Report on the Ocean and Cryosphere in a Changing Climate* [H.-O. Pörtner, D.C.
425 Roberts, V. Masson-Delmotte, P. Zhai, M. Tignor, E. Poloczanska, K. Mintenbeck, A. Alegria, M. Nicolai,
426 A. Okem, J. Petzold, B. Rama, N.M. Weyer (eds.)]
- 427 Hoelzle, M., Barandun, M., Bolch, T., Fiddes, J., Gafurov, A., Muccione, V., et al. (2019). *The status and
428 role of the alpine cryosphere in Central Asia*. doi:10.4324/9780429436475-8

- 429 Hori, M., Aoki, T., Tanikawa, T., Motoyoshi, H., Hachikubo, A., Sugiura, K., et al. (2006). In-situ
430 measured spectral directional emissivity of snow and ice in the 8–14 micrometer atmospheric window.
431 *Remote Sensing of Environment* 100, 486 – 502
- 432 [Dataset] IDAWEB (2019). Meteoswiss, federal office of meteorology and climatology. [Available at
433 <https://gate.meteoswiss.ch/idaweb/login.do>, accessed 2019-10-01]
- 434 Immerzeel, W. W., Lutz, A. F., Andrade, M., Bahl, A., Biemans, H., Bolch, T., et al. (2019). Importance
435 and vulnerability of the world's water towers. *Nature* 577, 364 – 369. doi:10.1038/s41586-019-1822-y
- 436 Meteoblue (2020). Climate schwarzsee [Available at https://www.meteoblue.com/en/weather/historyclimate/climatemodeled/schwarzsee_switzerland_11790334, accessed 2019-10-01]
- 437 Mölg, T. and Hardy, D. R. (2004). Ablation and associated energy balance of a horizontal glacier surface
438 on kilimanjaro. *J. Geophys. Res.-Atmos.* 109, 1–13. doi:10.1029/2003JD004338
- 439 Nüsser, M., Dame, J., Kraus, B., Baghel, R., and Schmidt, S. (2019a). Socio-hydrology of artificial glaciers
440 in ladakh, india: assessing adaptive strategies in a changing cryosphere. *Regional Environmental Change*
441 doi:10.1007/s10113-018-1372-0
- 442 Nüsser, M., Dame, J., Parveen, S., Kraus, B., Baghel, R., and Schmidt, S. (2019b). Cryosphere-Fed
443 Irrigation Networks in the Northwestern Himalaya: Precarious Livelihoods and Adaptation Strategies
444 Under the Impact of Climate Change. *Mountain Research and Development* 39. doi:10.1659/
445 MRD-JOURNAL-D-18-00072.1
- 446 Oerlemans, J. and Knap, W. H. (1998). A 1 year record of global radiation and albedo in the
447 ablation zone of morteratschgletscher, switzerland. *Journal of Glaciology* 44, 231–238. doi:10.
448 3189/S0022143000002574
- 449 Scherrer, S. C. (2020). Temperature monitoring in mountain regions using reanalyses: lessons from the
450 alps. *Environmental Research Letters* 15, 044005
- 451 Schmidt, L. S., Aðalgeirs ðóttir, G., Guðmundsson, S., Langen, P. L., Pálsson, F., Mottram, R., et al. (2017).
452 The importance of accurate glacier albedo for estimates of surface mass balance on vatnajökull: evaluating
453 the surface energy budget in a regional climate model with automatic weather station observations. *The
454 Cryosphere* 11, 1665–1684. doi:10.5194/tc-11-1665-2017
- 455 Tetens, O. (1930). Über einige meteorologische begriffe. z. *Geophys.* 6, 297–309
- 456 Unger-Shayesteh, K., Vorogushyn, S., Farinotti, D., Gafurov, A., Duethmann, D., Mandychev, A., et al.
457 (2013). What do we know about past changes in the water cycle of central asian headwaters? a review.
458 *Global and Planetary Change* 110, 4 – 25. doi:10.1016/j.gloplacha.2013.02.004. Water in Central Asia
459 – Perspectives under global change
- 460 Wangchuk, S. (2014). Ice stupa artificial glaciers of ladakh [Available at www.indiegogo.com/projects/ice-stupa-artificial-glaciers-of-ladakh#/, accessed 2019-10-01]
- 461 Wangchuk, S. (2015a). The good news at ice stupa 24th january 2015 [Available at <http://icestupa.org/news/the-good-news-at-ice-stupa>, accessed 2019-10-01]
- 462 Wangchuk, S. (2015b). Ice stupa artificial glacier inaugurated
463 5th of march 2015 [Available at <http://icestupa.org/news/ice-stupa-artificial-glacier-inaugurated-5th-of-march>, accessed
464 2019-10-01]
- 465 Wangchuk, S. (2015c). Ice stupa surpasses guiness world record [Available at <http://icestupa.org/news/ice-stupa-surpasses-guinness-world-record>, accessed 2019-10-01]
- 466 Wangchuk, S. (2015d). Ice stupa way of celebrating a special day [Available at <http://icestupa.org/news/ice-stupa-way-of-celebrating-a-special-day6th-of-ju>, accessed
467 2019-10-01]

- 474 2019-10-01]
- 475 Wangchuk, S. (2015e). World water day at ice stupa [Available at <http://icestupa.org/news/world-water-day-at-ice-stupa>, accessed 2019-10-01]
- 476
- 477 WMO (2018). *Guide to Instruments and Methods of Observation* (World Meteorological Organization ;
- 478 2018 (2018 Edition))
- 479 Woolf, H. M. (1968). *On the Computation of Solar Elevation Angles and the determination of sunrise and*
- 480 *sunset times* (National Aeronautics and Space Administration)
- 481 Zhou, S., Kang, S., Gao, T., and Zhang, G. (2010). Response of zhadang glacier runoff in nam co basin,
- 482 tibet, to changes in air temperature and precipitation form. *Chinese Science Bulletin* 55, 2103–2110.
- 483 doi:10.1007/s11434-010-3290-5